



Simulation and analysis of electron beam welding residual stress in thin-walled high-temperature alloy aeroengine structures

Xiuli Shen^{1,2} · Kun Gao^{1,2} · Shaojing Dong^{1,2}

Received: 23 October 2019 / Accepted: 31 March 2020 / Published online: 23 April 2020
© Springer-Verlag London Ltd., part of Springer Nature 2020

Abstract

Electron beam welding (EBW) is widely used to connect thin-walled high-temperature alloy structures in aeroengines. However, the residual stress and deformation caused by the high-temperature gradients generated during welding would affect the rigidity, dimensional stability, and fatigue resistance of the welded structures. The study reported here used a model combining ellipsoidal and Gaussian rotating body heat sources to undertake a numerical simulation of the temperature and residual stress generated during the EBW process. The model was systematically refined by observing and measuring the molten pool morphology. The error rates for key dimensions determining the molten pool shape were less than 6%. With a microscope-based examination, the energy distribution characteristics were detected by the microstructure analysis of grain type and size in different regions to verify the viability of the heat source model. The residual stress of a butt welding was simulated by the proposed heat source model based on the full consideration of a full-loop thin-walled combustor casing structure and material properties. It was found that the average errors for longitudinal and transverse residual stresses of welded joints and their adjacent areas were 10% and 12%, respectively, by comparing with the experimental results. Simultaneously, the low cycle fatigue life of the welded combustor casing would be decreased by 32% considering the influence of welding residual stress. These conclusions can be used as a basis for studying the integrity of thin-walled welded structures in aeroengines.

Keywords Electron beam welding · Welding heat source · Welding residual stress · Aeroengine · Thin-walled welded structure

Highlight

Advanced application background: Design and manufacture of high thrust-weight ratio aeroengines.

Advanced materials for aeroengines: Nickel-base high-temperature alloy (GH4169).

Advanced welding technology: Electron beam welding, a combined ellipsoidal and Gaussian rotating body heat source model.

Application background: Thin-walled welded structures in aeroengines, a full-loop combustor life prediction.

Research method: Numerical modeling, experimental verification, combination of macroscopic and microscopic analysis.

✉ Shaojing Dong
dshj0321@163.com

Xiuli Shen
shxl606@buaa.edu.cn

Kun Gao
gaokun@buaa.edu.cn

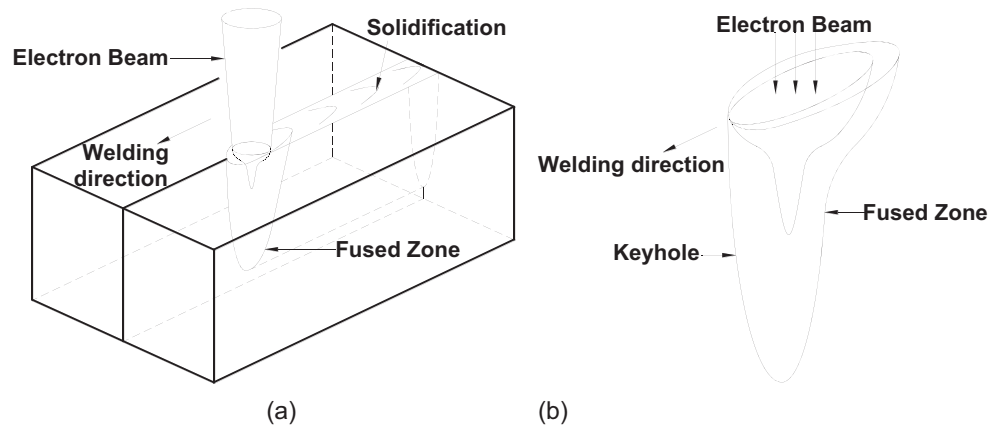
¹ School of Energy and Power Engineering, Beihang University, Beijing 100191, China

² Beijing Key Laboratory of Aero-Engine Structure and Strength, No. 37 Xueyuan Road, Haidian District, Beijing 100191, People's Republic of China

1 Introduction

Electron beam welding (EBW) characteristically produces a high energy density, a high aspect ratio, a small heat-affected zone (HAZ), and limited thermal deformation. It is suitable for welding almost all metals, but is especially effective for superalloys. As a result, it is universally used for the manufacture of high-temperature alloy structures in aeroengines [1]. Examples here include thin-walled disc-shaft structures such as the high-pressure compressor rotor in the Trent 600/700 engines; the high-pressure compressor disc and rear axle in the RB211 and PW4000 engines [2]; and the thin-walled casing structures such as the combustor casing in the CFM56 engine and the rear turbine casing in the BR710 and GE series engines [3]. As EBW is a form of fusion welding, it inevitably results in residual stress. The gas pressure typically present in high-temperature environments can subject thin-walled structures to significant amounts of radial stress. Any residual stress in such structures therefore tends to make them unstable [4]. The residual stress generated by EBW and the working stress caused by other loads can be superimposed on each

Fig. 1 The EBW process. **a** Welding process. **b** Keyhole effect [26]



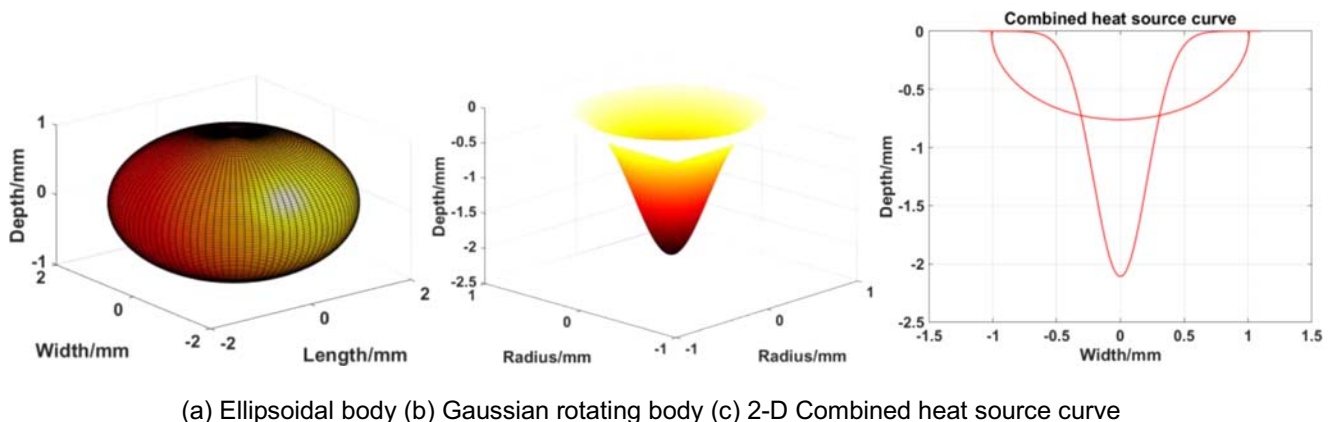
other, leading to secondary deformation and a redistribution of the residual stress. This can reduce the rigidity and dimensional stability of thin-walled structures, affect their fatigue and buckling strength, and limit their resistance to creep cracking when they are subjected to high temperatures and cyclic stress [5]. Therefore, a significant amount of research has focused on the influence of the welding process on the life of thin-walled structures such as combustor casing.

The thermal welding process can cause grain unevenness. This is a typical microscopic characteristic of materials after EBW. The key macroscopic consequences are (1) residual stress, arising from the temperature gradient [6] and (2) residual deformation, which is caused by solidification of the fusion joint [7]. Accurate simulation has therefore become an important part of the research regarding welding processes. How the microstructures and mechanical properties of welded joints evolve can be studied by simulating welding heat sources, temperature fields, and residual stress. This can also offer better insight into the impact of the welding process on the strength of welded joints and fatigue life of welded components.

Various heat source models have been developed for welding simulation. Pavelic et al. [8] were the first to establish a normal Gaussian distributed surface model for simulation. This captures the transmission of external heat from the

surface to each part of a welded component. However, welding methods such as EBW have a high penetration depth. So, this model cannot adequately describe the loading of the heat flow into the depth of a material. Goldak et al. [9] have proposed a double ellipsoidal distributed volumetric heat source model. This allows for the transmission of heat to each part of a welded component after internal heat generation. It is better at simulating the temperature distribution through the thickness of a material, but it ignores longitudinal heat flow. The equivalent conical heat source model, proposed by Bardel et al. [10], ignores the possibility of ablation at the front edge of a molten pool. Its boundary curve is also at odds with the results produced in actual experiments.

The internal heat flux density characterized by the abovementioned single heat source models is consistent with the actual heat flux density found in weld fusion lines. However, they do not accurately simulate the “nail-shaped” cross-section that forms near the surface of the molten pool. This is known as the keyhole effect [11]. This “nail-shaped” weld profile is extremely common in deep-welding approaches such as EBW. So, models that combine two types of heat source offer higher precision when simulating the shape of the molten pool [12]. Ziolkowski et al. [13] have proposed a combined heat source model that considers the



(a) Ellipsoidal body **(b)** Gaussian rotating body **(c)** 2-D Combined heat source curve

Fig. 2 Heat source model. **a** Ellipsoidal body. **b** Gaussian rotating body. **c** 2-D combined heat source curve

Seebeck effect (the generation of electricity at the point where two different materials with different temperatures meet). Their model simplifies the heat conduction problem into a static convection conduction problem. This limits the size of the heat source in the direction of its movement. Although this captures the characteristics of a high aspect ratio and the Seebeck effect, it does not simulate variations in the transient temperature field during the welding process. Petrov and Tongov [14] developed a combined heat source model that superimposes a circular surface heat source upon a cylindrical heat source, which takes into account the welding parameters. Here, though, the heat source model only reflects the general characteristics of welded joint morphology. There has been no detailed study of the heat flow radius throughout the depth of a joint. This makes it impossible to describe the molten pool using existing parameters. Ferro et al. [15] have proposed a combined spherical and conical heat source model that can simulate the shape of the weld zone with reasonable accuracy. However, its precision could be improved by more accurately constraining the boundary conditions for heat conduction and displacement of the welded component.

EBW has a characteristically high aspect ratio and a small HAZ and produces limited thermal deformation. Nonetheless, there can still be significant residual stress because of the huge temperature gradient it generates. This can have a detrimental effect upon the mechanical properties of the welded joint. Maurer et al. [16] studied the tensile strength of welded joints at different energy input levels. They found that the mechanical properties of the welding zone vary enormously according to the EBW process parameters. This makes it important to accurately assess the influence of the EBW process on the magnitude of residual stress and its distribution, which in turn determines the accuracy of other analyses and predictions, such as fatigue life. Thus, drawing upon research by Sun and Karppi [17], Venkata et al. [18] used neutron diffraction to measure the distribution of residual stress in a welding zone. They undertook a finite element analysis of a two-dimensional model, then applied the predicted residual stress to a three-dimensional model to study stress relaxation. The main limitations of this method are the high cost of neutron diffraction tests and the stringent requirements they placed upon test environments. The size of the samples is also restrictive, so universal application of the approach is impossible. Smith et al. [19] adopted a deep-hole drilling (DHD) method to measure the distribution of residual stress in thick plates welded using EBW. However, this is not applicable to the residual stress testing of thin-walled structures. Lacki et al. [20] studied EBW-induced thermo-mechanical phenomena by establishing a cross-sectional model of the molten zone. Having used the model to calculate the residual stress, they compared their results with x-ray diffraction measurements. This method enables non-destructive testing on the surface of samples. However, the measurement process is significantly affected by the surface state of the samples and the experimental environment. As the results

Table 1 Heat source model parameters

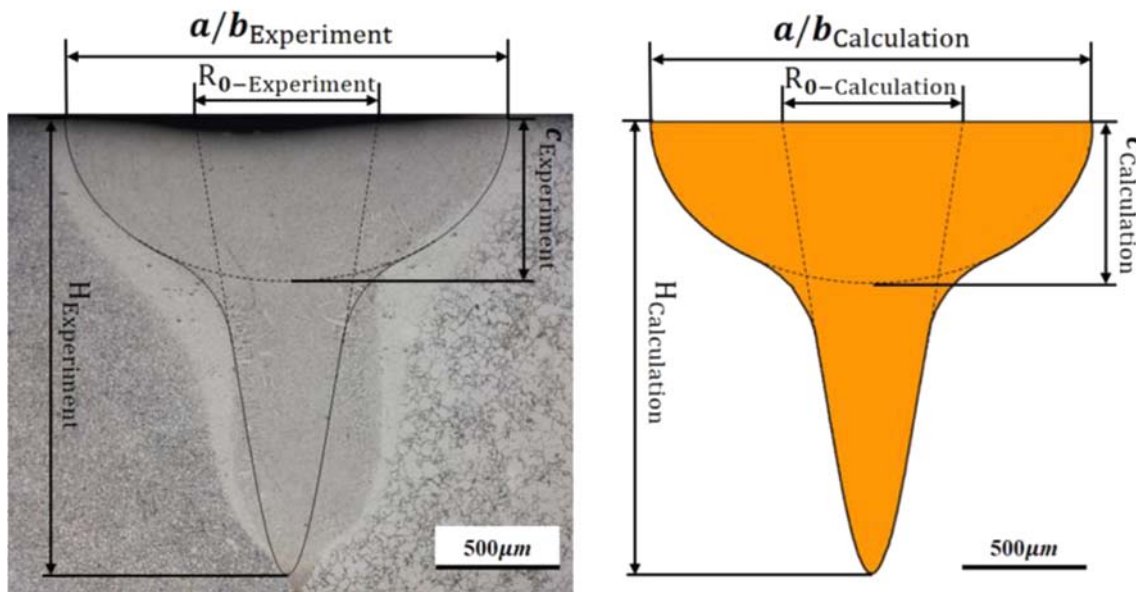
Parameter	Value
Energy proportionality coefficient, γ	0.1–0.5
Energy input efficiency, η	0.990
Heat flux concentration factor, α	1–3
Gaussian heat source radius, R_0/mm	0.460
Gaussian heat source height, H/mm	2.010
Half-axis length, a/mm	1.013
Half-axis length, b/mm	1.013
Half-axis length, c/mm	0.760

from this approach are more dispersive, it is better suited to the measurement of thin layers and tip cracking defects. Elliot [21] investigated variations in the welding stress field by observing changes in the microstructure of welded joints related to changes in EBW parameters. This approach allows for a detailed description of the microstructural features, but has a high computational cost. It also requires a large amount of experimental data to verify the consistency of the results. A further limitation is that a single physical model cannot accurately predict residual stress in general. Simulating welding thermal processes and calculating post-weld residual stress are equivalent to undertaking a welding process and engaging in post-weld analysis. By establishing the relationship between welding process parameters and welding residual stress, reasonable measures can then be taken to control against future welding residual stress and deformation.

In the present study, a combined heat source model for EBW was studied and the welding process was simulated by finite element method (FEM). This paper aims at developing a precise combined heat source model that can conform to specific welding parameters to establish the relationship between EBW process parameters and residual stress, so as to study the influence of EBW residual stress on thin-walled combustor casing in aeroengines. Hence, the heat source model was iteratively calibrated on the basis of the experimental results and further verified through macro-microscopic analysis of the molten pool morphology. Based on a numerical simulation and experimental validation of the residual stress in a nickel-based superalloy welded plate without heat treatment, the low-cycle fatigue life of a combustor casing was predicted by adding welding residual stress. The present research can be

Table 2 Chemical compositions of the Ni-based superalloy GH4169 (wt%)

Material	Elements							
GH4169	Ni	Cr	Nb	Mo	Al	Ti	Mg	Fe
	54.10	19.39	5.21	3.05	0.53	1.02	0.01	Bal.



(a) Molten pool morphology (b) Fitted curve of the molten pool boundary

Fig. 3 Weld profile optimization. a Molten pool morphology. b Fitted curve of the molten pool boundary

considered as a relatively complete method for establishing the heat source model under different parameters, calculating the accurate welding residual stress, and grasping the influence of the residual stress on the welded structures.

2 A heat source model for electron beam welding

2.1 Heat source modeling

A heat source model is key to the numerical simulation of welding. Its capacity to properly describe the characteristics of heat energy and its distribution through the welded components determine the subsequent accuracy of the calculated temperature, stress, and deformation. Figure 1 a shows a schematic diagram of the EBW process. An EBW weld is small but its simulation involves a large amount of mesh and simplified processing. This is because, where there is a “keyhole effect” [22] (Fig. 1b), the construction of the heat source typically demands a fine mesh. This significantly increases the amount of calculation. However, numerous studies have

shown that calculation models that ignore the “keyhole effect” are still able to meet the requirements of engineering applications when predicting the stress and strain associated with high-energy beam welding [23–25].

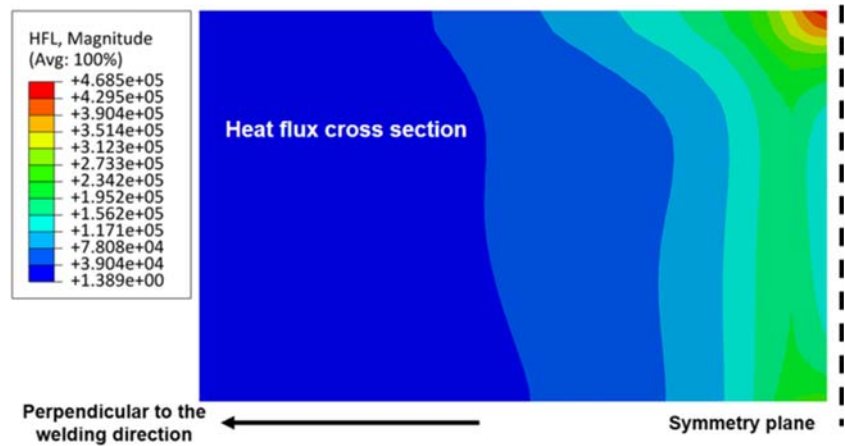
In this study, a model combining ellipsoidal and Gaussian rotating body heat sources was used to simulate the EBW mechanism and its characteristically large penetration depth. The model is also able to incorporate some of the characteristics of the keyhole effect. Additional verification of the heat source model was undertaken through microscopic observation of the molten pool. The combined heat source model reflects not only the general geometric features of an electron beam welded joint but also the radius of the heat flow throughout its depth. It also accurately expresses the molten pool morphology relating to different welding parameters.

For high-energy particle beam welding processes such as EBW, an ellipsoidal heat source is effective at simulating the heat flux distribution on the surface of the welded component. Meanwhile, the energy of a Gaussian rotating body heat source suitably attenuated in a specific form in the depth direction is better able to simulate the depth and width of a weld. The total power of the combined heat source [27] was

Table 3 Key dimension errors for the molten pool

Key dimensions (mm)	Calculation	Experiment	Error (%)
Half-axis length of ellipsoid heat source, a/b	1.013	1.073	5.92
Half-axis length of ellipsoid heat source, c	0.760	0.735	3.29
Gaussian heat source radius, R_0	0.460	0.455	1.09
Gaussian heat source height, H	2.010	2.100	4.47

Fig. 4 Numerical simulation results for the welding heat flux density



$$\Phi = \Phi_E + \Phi_G = \eta \cdot IU \tag{1}$$

where η is the energy input efficiency; I is the acceleration voltage; and I is the electron beam current. Φ_E and Φ_G are the power of the ellipsoidal heat source and the Gaussian rotating body heat source, respectively, which can be specified as follows:

$$\Phi_E = \gamma \cdot \Phi \tag{2}$$

$$\Phi_G = (1-\gamma)\Phi \tag{3}$$

where γ is the energy proportionality coefficient of the ellipsoidal heat source.

Drawing upon Fourier’s law, the EBW temperature field control equation [28] is

$$\rho_{CL} \cdot \partial T / \partial t = \partial(k_x(T) \cdot \partial T / \partial x) / \partial x + \partial(k_y(T) \cdot \partial T / \partial y) / \partial y + \partial(k_z(T) \cdot \partial T / \partial z) / \partial z + \dot{\Phi}_V \tag{4}$$

where ρ is the material density; T is the temperature; $\dot{\Phi}_V$ is the internal heat source intensity, which is related to the power of the body heat source; c_L is the modified specific heat capacity;

and $k_x(T)$, $k_y(T)$, and $k_z(T)$ are the coefficients of thermal conductivity in the x , y , and z directions. For a high-temperature alloy like GH4169, the relationship $k_x(T) = k_y(T) = k_z(T)$ makes sense.

The ellipsoidal heat source energy density [9] is

$$q_E(r) = (6\sqrt{3}\alpha\Phi_E) / (\pi^{3/2}abc) \cdot \exp(-3((x/a)^2 + (y/b)^2 + (z/c)^2)) \tag{5}$$

where a , b , and c are half-axis lengths; α is a heat flow concentration factor; and x , y , and z are the internal coordinates of the heat source, as shown in Fig. 2a.

The Gaussian rotating body heat source energy density [29] is

$$q_G(r) = (9\Phi_G) / (\pi R_0^2 H (1 - 1/e^3)) \cdot \exp(-9(x^2 + y^2) / (R_0^2 \cdot \log(H/z))) \tag{6}$$

where R_0 is the heat source radius; H is the heat source height; and x , y , and z are the internal coordinates of the heat source, as shown in Fig. 2b. Figure 2c shows the two-dimensional combined heat source curve.

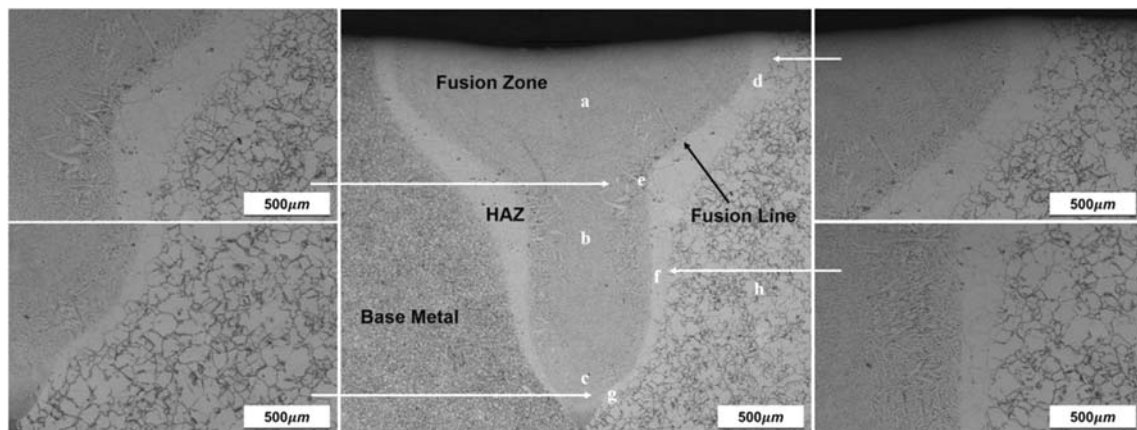


Fig. 5 Microscopic observations of welding zone

2.2 Model parameters and material properties

Within the same welding process, the parameters U , α , γ , and η are relatively fixed, while R_0 , H , a , b , c , and I vary according to the material and other process-related parameters. In this study, the specific welding parameters used were an acceleration voltage of 85 kV, an electron beam current of 7 mA, and a welding speed of 0.013 m/s. The relevant parameters for the heat source model after calculation are shown in Table 1. H is roughly proportional to the electron beam current. Note that the maximum temperature in the center of the molten pool can exceed 3000 °C. So, when studying the weld aspect ratio, the melting point of the nickel-based superalloy was taken as the limit for the molten pool.

To meet environmental and manufacturing requirements, combustor casings are usually made of the nickel-based superalloy GH4169. This material offers a good overall performance across a wide range of temperatures, especially as its thermal and mechanical properties [30] are functions of temperature. In addition, its yield strength ranks first for wrought superalloys below 650 °C and it is widely used in aerospace components. Table 2 lists the chemical compositions of GH4169 [31].

2.3 Numerical verification

Two pieces of nickel-based wrought superalloy were butt welded by vacuum EBW. The metallographic structure in the weld zone (Fig. 3a) was then examined using a Carl Zeiss microscope after polishing and etching. Key dimensions such as width and depth are marked in Fig. 3. By comparing the observed weld profile with the fitted curve of combined heat source model (Fig. 3b), the model was checked and optimized to obtain the most accurate and appropriate heat source parameters possible. The errors in the key dimensions are shown in Table 3. Comparing the experimental results with the calculated results, it was found that the errors related to the key dimensions determining the shape of the molten pool were below 6%. It should be noted that the bottom half of the weld in the microscopic observation is obviously asymmetrical and wider than the corresponding position of the heat source model. This may be caused by the ignorance of the coupling phenomena of fluid flow and heat transfer in the model. The coupling phenomena mainly include the following physical effects [32]: (1) gravity and wetting effects within the partially melted metal and underlying base metal; (2) flow within the melt pool generated by thermal buoyancy forces and the Marangoni effect associated with temperature-dependent surface tension; (3) non-uniform material microstructure.

A thermodynamic simulation of high-temperature alloy EBW was carried out using the Abaqus software platform. The DFLUX subroutine written in Fortran defined Formulas

(1)–(6) and the parameters in Table 1, and also defined current, voltage, welding speed, and other process parameters during EBW. After a geometric model was built in the part module, it could be important in high-precision work of this nature to define the material properties of GH4169, such as conductivity, density, expansion, plastic, and specific heat. The extremely important step was to set transient heat transfer in the load module to simulate the welding process and the cooling process, respectively. In the situation of heat transfer, it was necessary to select an 8-node linear heat transfer brick (DC3D8) and the temperature-displacement coupling type. We could select output data in the field output module as required to obtain the results of welding temperature field and heat flux. It can be seen from the numerical results that the combined heat source model accurately reflected the characteristics of the EBW heat source. The contour curve of the heat flux density has a very obvious “keyhole” shape (Fig. 4). The size and gradient of the molten pool were very close to the actual weld.

The results show that the simulation of the molten pool closely matched the actual weld contour. This confirms the validity of the thermodynamic and geometric parameters for the combined heat source model. Thus, a combined ellipsoidal and Gaussian rotating body heat source model is able to accurately describe the heat flux distribution characteristics present during EBW and can serve the calculation of a valid temperature field distribution.

By analyzing the effect of a high-energy particle beam on a high-temperature alloy during EBW, it was possible to establish a mathematically similar model of the combined heat source model. The model parameters were then adjusted and optimized according to actual weld morphology to arrive at a more accurate version of the combined heat source model. A simulation of how the heat source moved during the welding process was obtained using FEM and the geometry of the molten pool was also simulated. This confirmed the feasibility of the combined heat source model and the accuracy of the thermodynamic parameters. The calculated transient temperature was then able to serve as boundary conditions when calculating the EBW residual stress.

2.4 Microstructure verification

To further verify the viability of the heat source model, a microscope-based examination was undertaken. An EBW metallographic sample was cut along the direction perpendicular to the weld, then ground, polished, and etched to prepare it for observation. The microstructure of the high-temperature alloy welded joint was examined using an optical microscope. Key areas such as the fusion line and the HAZ were further enlarged and inspected (see Fig. 5, where the letters correspond to the different welding zones shown in Fig. 6). By observing the grain size, growth direction, and other characteristics, the

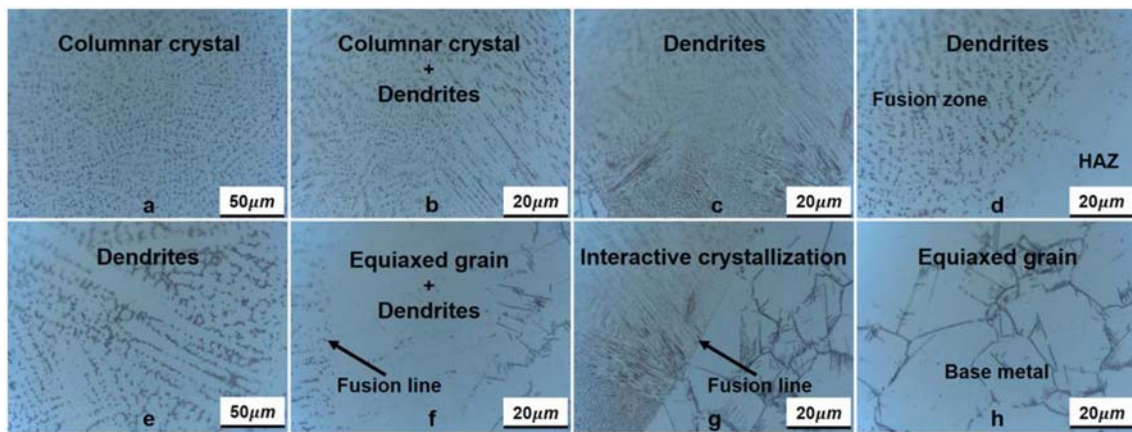


Fig. 6 Microstructure in different welding zones

energy transfer direction and distribution characteristics of the thermal process were indirectly analyzed to verify the rationality of the heat source model.

Figures 6a–h show the microstructure of the welded samples at different locations. Figure 6a shows that the metal at the weld center and near the plate surface had a cast structure, with the crystallized grains near the fusion zone being co-integrated with those in the HAZ and developing a dendritic shape (see Fig. 6e). In other words, the crystallization of the metal in the fusion zone grows from the semi-molten grains of the base metal towards the center of the weld, as shown in Fig. 7. This phenomenon can be explained by the fact that if the direction in which the crystallized grains grow most easily matches the direction in which the heat is dissipating most rapidly, this will favor their growth. When their orientation is not conducive to their formation, their growth is suppressed. This is called selective growth [33] and leads to the growth of columnar crystals. The characteristic of heat source model in this paper is that heat concentrates locally in the center and then transfers around. The area where the electron beam acted had a very high heat flux density, and there was a huge heat flux density gradient away from the electron beam and close to the HAZ. This made the grain grow along the direction of heat dissipation, which resulted in the growth characteristics of the grain in the melting zone as shown in Fig. 5.

As the cooling rate after welding is rapid, the recrystallized dendrites formed at this stage are retained. The gradient of the upper weld line at this point is large, so the cross-section of the molten zone is approximately fan-shaped. However, the lower weld becomes long and narrow, and the cross-section is approximately the nail body. Therefore, the heat source model in this paper needs ellipsoid and Gaussian shape to reflect these two geometric features. In comparison to the upper part of the weld, there are fewer dendrites in the middle of the weld (Fig. 6b) and more columnar crystals. As this region is located half-way through the thickness of the plate, the growth of the columnar crystals and heat dissipation makes the

liquid in the molten pool fall below melting point and the heat ceases to dissipate in any one clear direction. The relatively slow cooling rate provides the formation of columnar crystals inside the weld line, resulting in a decrease in the number of dendrites at the center. The crystallized grains in the middle of the HAZ (Fig. 6f) are noticeably larger, but they are still smaller than those in the HAZ near the surface layer of the sample. This is because, while the middle part cools down more slowly than the surface, the total heat input is less than it is at the surface. As with the upper part of the weld, a certain number of dendrites are retained in the lower part of the weld center (see Fig. 6c). The lower surface of the plate cools rapidly, so, the fine crystallized grains remain in the weld center and their growth in the lower portion of the HAZ is suppressed (Fig. 6g). As a result, they remain more or less the same size. All these characteristics are in accordance with the energy transfer direction and distribution characteristics in the process of electron beam welded thin-walled plate, thereby further underscoring the viability of the proposed heat source model.

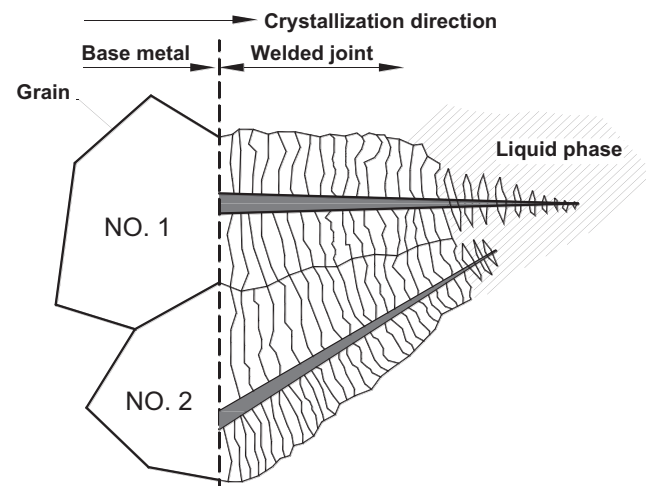


Fig. 7 Interactive crystallization of the base metal and weld metal

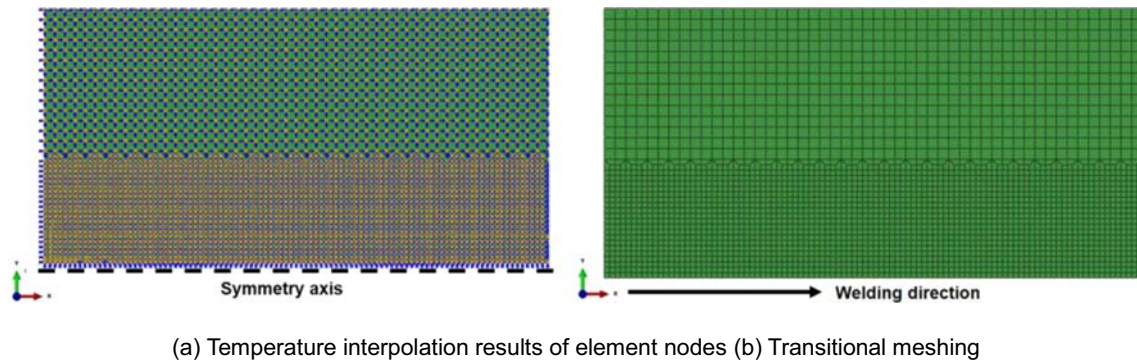


Fig. 8 Finite element technique for EBW simulation. **a** Temperature interpolation results of element nodes. **b** Transitional meshing

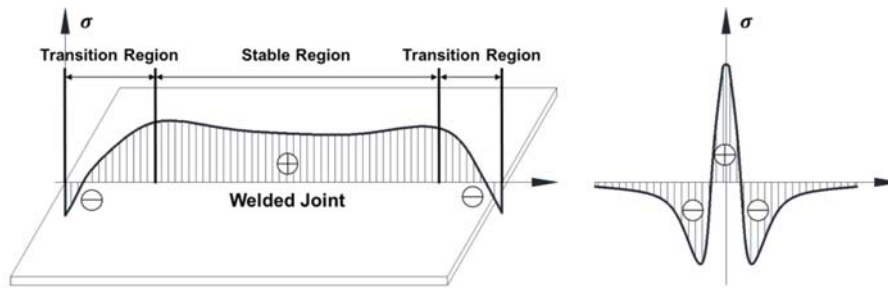
3 Residual stress in electron beam welding

3.1 Numerical simulation of EBW residual stress

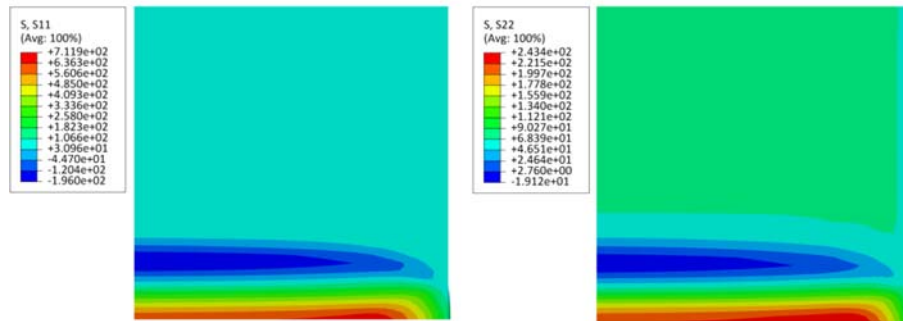
The nature of residual stresses can also be discussed in terms of their characteristic length, at which the stresses equilibrate. The welding residual stress studied in this paper is the type I residual stress [34, 35], that is, the long-term stress balance on the macro-scale. This stress can be estimated by a continuum model that ignores the polycrystalline or polyphase properties of the material, and it is usually calculated by FEM.

During FEM, the stress is caused by the existence of a thermal field, while the thermal solution process is

independent of the stress state; that is, the stress depends on the heat generation, while the heat does not depend on the displacement. Two processes need to be analyzed: heat transfer and stress analysis. The results of thermal analysis, such as the function of temperature-position and temperature-time, were read into the stress analysis as a predefined field. Therefore, a non-linear transient thermal analysis was performed using a combined heat source to calculate the butt welding temperature of two $100 \times 50 \times 2$ mm GH4169 plates. In the fully coupled thermo-stress analysis of ABAQUS/Standard, the thermal results were applied to the element nodes (see Fig. 8a) as a known external load to generate thermal strain.



(a) Theoretical residual stress trend along the weld (b) Theoretical residual stress trend perpendicular to the weld



(c) Simulation results for the longitudinal residual stress (d) Simulation results for the transverse residual stress

Fig. 9 Theoretical trend and calculated results of residual stress on the welded plate surface. **a** Theoretical residual stress trend along the weld. **b** Theoretical residual stress trend perpendicular to the weld. **c** Simulation

results for the longitudinal residual stress. **d** Simulation results for the transverse residual stress

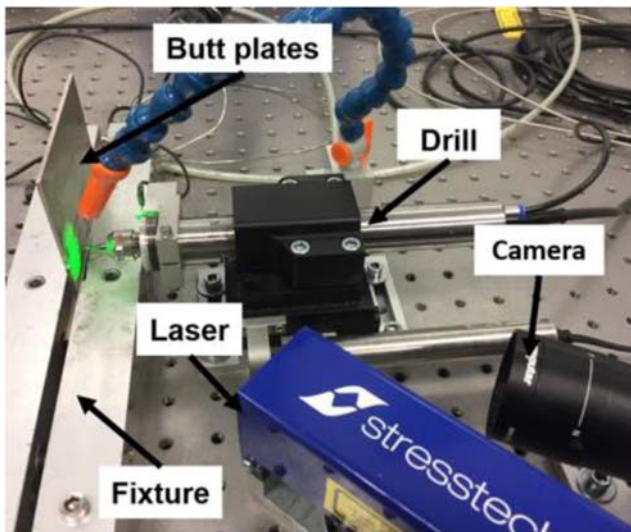


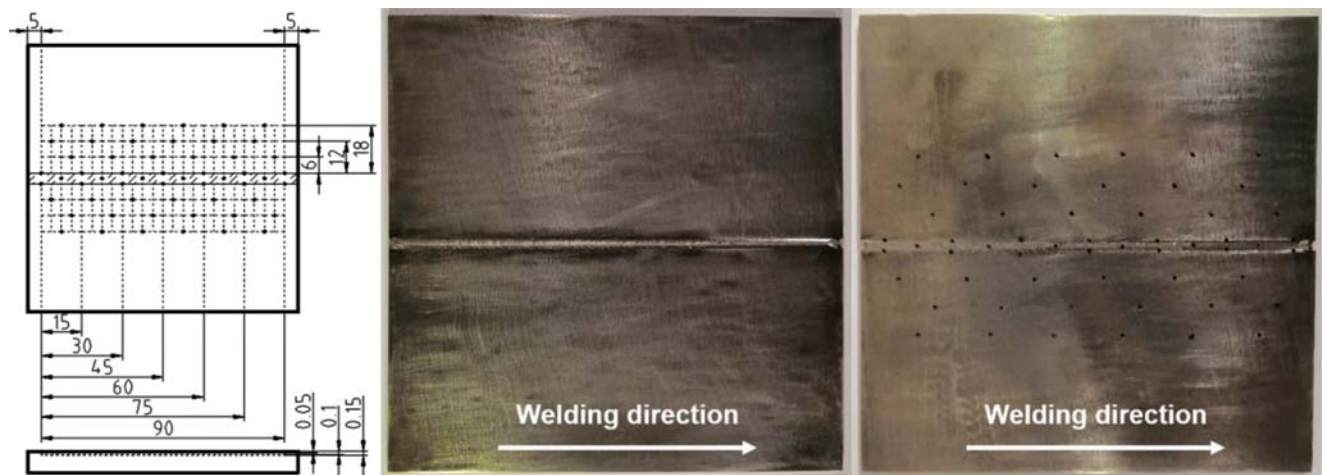
Fig. 10 Residual stress measurement system

In order to reduce the computational cost, the calculation was performed using a half of the plate due to the symmetry principle. A transitional meshing technology (see Fig. 8b) was applied to reduce the total number of elements and increase the element density of the weld and its adjacent area. It is necessary to establish a static structural analysis step as required, including heating and cooling processes. The initial boundary conditions mainly include initial temperature and displacement constraints. The initial temperature of the whole model is generally room temperature. To ensure that the model did not exhibit any rigid-body displacement, a symmetrical boundary condition was applied to the center plane of the plate. The translational freedom of the plate surface nodes was then constrained in the *X*, *Y*, and *Z* directions. This is consistent with the clamping

typically used in actual welding processes. The material parameters are consistent with those in Section 2.3. The timing of the loading during the thermal analysis is consistent with the action of the heat source. A natural cooling time step was established to reduce the residual stress to a stable level. A sequential thermal coupling calculation was then conducted until a desired level of convergence was achieved. The residual stress field could then be obtained. Figure 9c and d are stress cloud diagrams for a quarter-symmetric model of the thoroughly cooled welded plate.

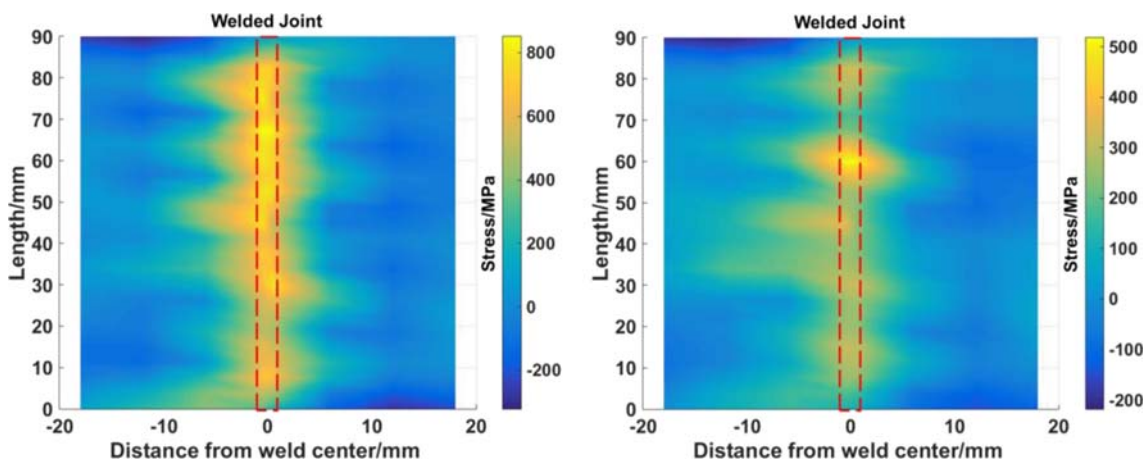
Welding residual stress can be divided into longitudinal residual stress and transverse residual stress [36] (see Fig. 9). Residual stress in a direction parallel to the weld axis is called S11 longitudinal residual stress. The asymmetrical temperature field generated during welding causes non-uniform expansion of the welded joint and thermoplastic compression around it. Shrinkage of the weld zone is limited during cooling and tensile stress is generated. When the welded joint has completely cooled, the tensile stress remains in the weld zone. Welding longitudinal residual stress has a relatively large stress value (see Fig. 9c). Stress perpendicular to the weld axis is called S22 transverse residual stress. This is more complicated than longitudinal stress. Transverse stress can be divided into two parts. One is the stress caused by the longitudinal shrinkage of the weld and its adjacent plastic deformation zone. The other is caused by transverse contraction of the weld and contraction in its adjacent plastic deformation zone happening at a different time to one another. The stress value for welding transverse residual stress is relatively small (see Fig. 9d).

Analysis of the mechanism for residual stress in welding has shown that residual stress along the centerline of a weld



(a) Distribution of test sites (b) Pre-measurement image (c) Post-measurement image

Fig. 11 Residual stress measurement plan. a Distribution of test sites. b Pre-measurement image. c Post-measurement image



(a) Longitudinal residual stress distribution (b) Transverse residual stress distribution

Fig. 12 Residual stress measurement results. a Longitudinal residual stress distribution. b Transverse residual stress distribution

increases as the distance from the weld’s starting point increases. There are three phases associated with this kind of residual stress: increasing stress, stability, and decreasing stress (see Fig. 9a). Looking at the S11 residual stress along the centerline of the weld in Fig. 9c, the value near the weld’s start point and end point was close to 0 or negative. The value in the middle of the weld line, however, was larger. Residual stress perpendicular to the centerline of the weld has been shown to decrease as the distance from the center of the weld increases. The relevant phases here are reducing stress, increasing stress, and stability (see Fig. 9b). As shown in Fig. 9d, the S22 residual stress followed the same tendency; i.e., the residual stress near the center of the weld was large. It then decreased to a negative value, before increasing and stabilizing around zero.

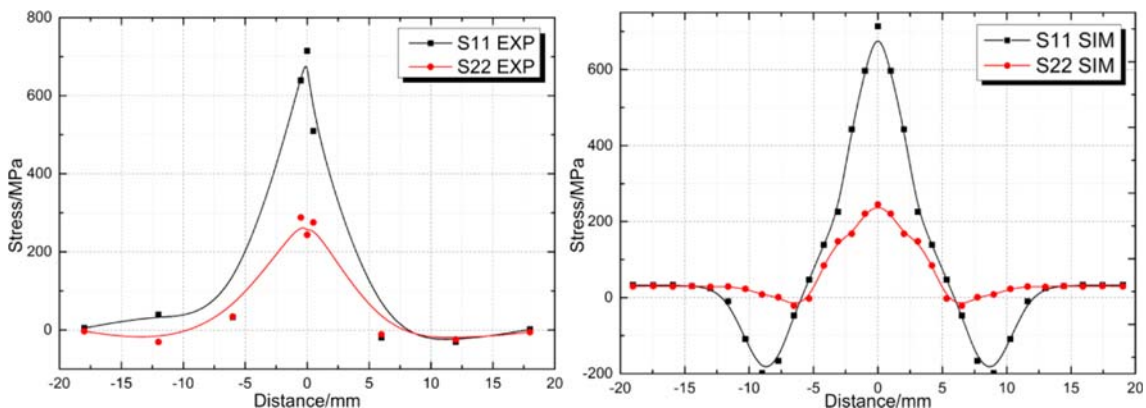
Due to the symmetry of the model, the computation can be reduced by focusing the analysis upon the cloud image of just a quarter of the plate. It can be seen that the simulated distribution of the EBW residual stress was the same as the

theoretical distribution. In the finite element-based simulation of the welded plate, the peak value for the S11 was 713.75 MPa and, for the S22, it was 245.02 MPa.

3.2 Measurement of welding residual stress

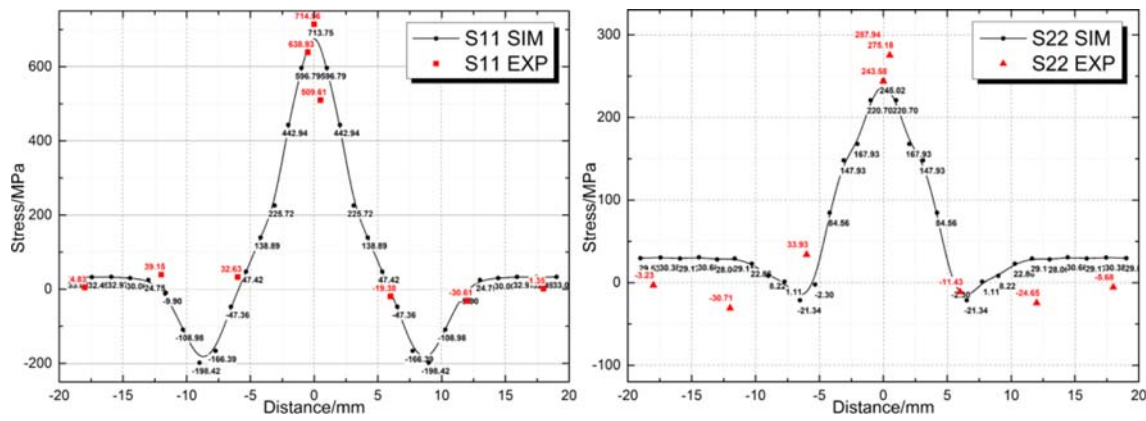
For the experiments reported here, a Prism borehole residual stress gauge based on digital imaging and electronic speckle pattern interferometry (EPSI) was used to measure the residual stress on the surface around the borehole. Figure 10 shows the residual stress measurement system. This device can measure the plane stress in material removed from the hole. The measurement error was within ± 2 MPa [37].

Drawing upon the variational law of residual stress, a measurement layout scheme was designed (see Fig. 11). The residual stress values at a depth of 0.05 mm, 0.10 mm, and 0.15 mm on the surface were measured. After averaging the measured values at different depths, MATLAB was used to visualize the results, as shown in Fig. 12.



(a) Fitted curve derived by the experimental data (b) Fitted curve derived by the simulated data

Fig. 13 Experimental measurement and numerical simulation of the residual stress. a Fitted curve derived by the experimental data. b Fitted curve derived by the simulated data



(a) Comparison of the longitudinal residual stress (b) Comparison of the transverse residual stress

Fig. 14 The measured and simulated values of residual stress. **a** Comparison of the longitudinal residual stress. **b** Comparison of the transverse residual stress

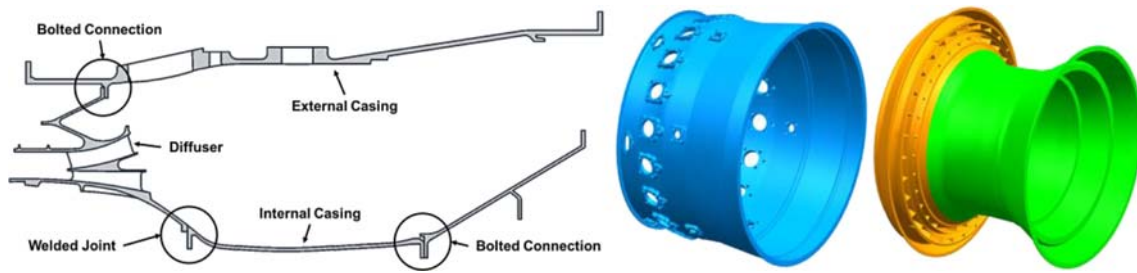
Table 4 Residual stress errors at different distances from the weld center

Distance/mm	-12	-6	-0.5	0	0.5	6	12	Mean	Min
S11 errors /%	101.56	117.13	2.56	0.11	28.59	71.16	98.01	59.87	0.1
S22 errors /%	193.88	138.17	19.13	0.59	15.38	216.96	216.96	85.34	0.6

With reference to the theoretical calculation of welding residual stress, a test measurement curve (Fig. 13a) and numerical calculation curve (Fig. 13b) were fitted for the results. Comparing the simulation results to the experimental measurements (Fig. 14), it can be seen that there was a large residual tensile stress in the region 5 mm from the center of the weld. This was a result of the longitudinal shrinkage in the weld being constrained. The maximum residual tensile stress was strictly limited to areas directly adjacent to the weld. As the distance from the center of the weld increased, the tensile stress gradually decreased and eventually transformed into compressive stress. This occurred in the region 5 to 12 mm from the center of the weld. As the distance continued to increase and approached the edge of the plate, the compressive stress started to stabilize and approached zero.

To assess the difference between the simulation and the experiment, errors in the longitudinal residual stress and transverse residual stress were calculated separately. The errors were calculated by selecting distances from the center of the weld of 0 mm, 0.5 mm, 6 mm, and 12 mm (see Table 4 and the residual stress measurement layout scheme in Fig. 11). It can be seen from the overall residual stress diagram (Fig. 14) that the simulation results were generally consistent with the experimental results. Note in particular that, in the direction perpendicular to the weld axis, the trends for the S11 (Fig. 14a) and S22 (Fig. 14b) were in good agreement.

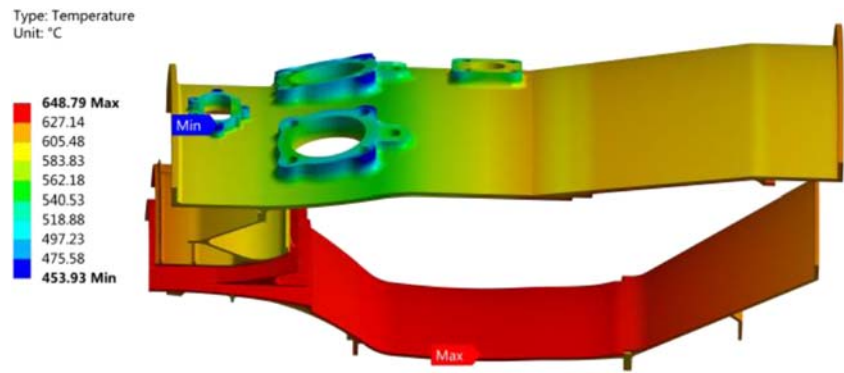
After analyzing the errors, it was found that the closer the point was to the weld center, the smaller the error. This was especially the case for the region up to 0.5 mm from the weld center. This is also a key location for studying the molten pool



(a) Meridian plane (b) External casing (c) Diffuser and internal casing

Fig. 15 Welded combustor casing. **a** Meridian plane. **b** External casing. **c** Diffuser and internal casing

Fig. 16 Temperature of welded combustor casing



and the HAZ. The larger errors in the region far from the weld center are largely a result of the measurement points in the weld zone being denser, while the ones further away from the weld were sparser, making the measurement interval larger. This can be seen in the residual stress measurement layout scheme in Fig. 11a. This led to a loss of accuracy in the residual stress data as the measurements moved away from the center of the weld. The limitations of the measuring instrument meant that the distance between each measuring point had a minimum value and this controlled where it was feasible to measure the residual stress. Thus, the measurement results were discontinuous.

The average errors for S11 and S22 were 10% and 12%, respectively. However, the errors for S11 and S22 at the weld center were only 0.1% and 0.6%, respectively. So, discounting the outliers, there was actually only a small error between the simulated stress values and the measured ones. This means that the simulation results are applicable to engineering practice and prove the feasibility of using a combined ellipsoidal and Gaussian rotating body heat source model to simulate the EBW process. The results also affirm the superiority of the model's capacity to reflect real welding conditions and improve the accuracy of numerical calculations.

3.3 Application example: the fatigue life of a welded combustor casing

According to the EBW heat source simulation and residual stress calculation, the low-cycle life prediction of welded combustor casing was also carried out in this study. A typical

combustor casing from a civil aviation engine was used as an example (see Fig. 15). Like the welded plate used in Section 2 above, the thickness of the casing was 2 mm, so the EBW parameters remain unchanged. Given the operational load spectrum during actual flights, including the temperature (see Fig. 16), pressure, and axial force. The welding residual stress was added into the welded joint calculations in the form of a boundary condition, and its specific value was consistent with the calculated results in Section 3.1.

The Manson–Coffin [38–40] formula shown in Eq. (7) was used to predict the low-cycle fatigue (LCF) life of the welded combustor casing:

$$\varepsilon_a = \sigma'_f (2N_f)^b / E + \varepsilon'_f (2N_f)^c \quad (7)$$

Here, ε_a is the strain range; N_f is the structural low-cycle fatigue life; σ'_f is the fatigue strength coefficient; ε'_f is the fatigue plasticity coefficient; b is the fatigue strength exponent; c is the fatigue plasticity exponent; and E is the elasticity modulus. The maximum equivalent stress and maximum deformation, together with the low-cycle fatigue value for a welded and non-welded casing, were calculated using FEM, as shown in Table 5.

The results show that the stress and deformation of the welded casing increased by 5.73% and 0.25% when compared with the non-welded casing. However, the low-cycle fatigue life decreased by 32%. This confirms that welding residual stress does affect the fatigue strength of thin-walled structures such as welded combustor casings and that it can reduce the low-cycle life of these kinds of components.

Table 5 Comparative stress, deformation, and LCF values for the combustor casing

Parameter	Max Von Mises stress/MPa	Max deformation/mm	LCF/cycles
Non-welded casing	930.53	8.13	21,345
Welded casing	983.81	8.15	14,520
Variation	5.73%	0.25%	–31.97%

4 Conclusions

The following conclusions can be drawn from this study:

- (1) A model combining ellipsoidal and Gaussian rotating body heat sources was designed and optimized to characterize EBW mechanism and its large penetration depth. The model can also reflect the keyhole effect of

EBW to some extent. Through a transient heat transfer simulation and microstructure observation experiments, a comparison between calculated and experimental results showed that the errors in key dimensions determining the molten pool shape were within 6%. Thus, the accuracy of the model is verified to be relatively high.

- (2) A sequential thermal coupling calculation was undertaken to calculate the welding residual stress, which was measured by the hole drilling method. It was found that the welding residual stress is limited to a region close to the center of the weld. The results of the numerical simulation and experimental measurements were consistent with the trends indicated by the theoretical curves. The closer it got to the center line, the smaller the error. In the region 0.5 mm to either side of the weld center, the average S11 and S22 residual stress errors were 10% and 12%, respectively, while those at the weld center were only 0.1% and 0.6%.
- (3) The calculation results of EBW temperature and residual stress regarding thin plate were used to predict the fatigue life of the combustor casing of an aeroengine. Compared with the non-welded casing, the equivalent stress and deformation of the welded casing increased by 5.73% and 0.25%, respectively, while the low-cycle fatigue life decreased by 32%. This confirms that welding residual stress does have an important effect on the thin wall structure such as the welded combustor casing in aeroengines.

Compliance with ethical standards

Conflict of interest We wish to draw the attention of the Editor to the following facts which may be considered as potential conflicts of interest and to significant financial contributions to this work.

We confirm that the manuscript has been read and approved by all named authors and that there are no other persons who satisfied the criteria for authorship but are not listed. We further confirm that the order of authors listed in the manuscript has been approved by all of us.

We understand that the corresponding author is the role contact for the editorial process (including Editorial Manager and direct communications with the office). She is responsible for communicating with the other authors about progress, submissions of revisions, and final approval of proofs. We confirm that we have provided a current, correct email address which is accessible by the corresponding author and which has been configured to accept email from The International Journal of Advanced Manufacturing Technology.

References

1. Qu S, Li Y, Ni JC, Yang S, Zhou GN (2015) Application of advanced welding technology in aeroengine. *Aeronaut Manuf Technol* 58(20):53–55 <http://www.amte.net.cn/CN/10.16080/j.issn1671-833x.2015.20.053>. <http://www.amte.net.cn/CN/article/downloadArticleFile.do?attachType=PDF&id=571>
2. Zhang L, Han XF, Wang L (2015) Welding process analysis of disk and shaft rotor component of commercial aeroengine. *Aeronautical Manufacturing Technology* 480(11):96–98 <http://www.amte.net.cn/CN/10.16080/j.issn1671-833x.2015.11.096>. <http://www.amte.net.cn/CN/article/downloadArticleFile.do?attachType=PDF&id=345>
3. Zhang L, Han XF, Wang L (2016) Application of welding process in commercial aeroengine. *Weld Join* 8:54–59 http://www.wanfangdata.com.cn/details/detail.do?_type=perio&id=hj201608012
4. Liu D, Zhou WB, Sun HB, Song J, Wu Q (2019) Residual stress field evaluation of the blank of a casing part. In *IOP Conference Series: Materials Science and Engineering* (Vol. 612, No. 3, p. 032168). IOP Publishing. <https://iopscience.iop.org/article/10.1088/1757-899X/612/3/032168/meta>. <https://iopscience.iop.org/article/10.1088/1757-899X/612/3/032168/pdf>
5. Jha AK, Arumugham S (2001) Metallographic analysis of embedded crack in electron beam welded austenitic stainless steel chemical storage tank. *Eng Fail Anal* 8(2):157–166. [https://doi.org/10.1016/S1350-6307\(00\)00003-0](https://doi.org/10.1016/S1350-6307(00)00003-0)
6. Zhan XH, Wu YF, Kang Y, Liu X, Chen XD (2019) Simulated and experimental studies of laser-MIG hybrid welding for plate-pipe dissimilar steel. *Int J Adv Manuf Technol* 101(5–8):1611–1622. <https://doi.org/10.1007/s00170-018-3066-7>
7. Węglowski MS, Blacha S, Phillips A (2016) Electron beam welding—techniques and trends—review. *Vacuum* 130:72–92. <https://doi.org/10.1016/j.vacuum.2016.05.004>
8. Pavelic V, Tanbakuchi R, Uyehara OA, Myers PS (1969) Experimental and computed temperature histories in gas tungsten-arc welding of thin plates. *Weld J Res Suppl* 48:296–305 <https://ci.nii.ac.jp/naid/10018019515/>
9. Goldak J, Chakravarti A, Bibby M (1984) A new finite element model for welding heat sources. *Metall Mater Trans B Process Metall Mater Process Sci* 15(2):299–305. <https://doi.org/10.1007/BF02667333>
10. Bardel D, Nelias D, Robin V, Pirling T, Perez M (2016) Residual stresses induced by electron beam welding in a 6061 aluminium alloy. *J Mater Process Technol*, 235. <https://doi.org/10.1016/j.jmatprotec.2016.04.013>
11. Wang YJ, Fu PF, Guan YJ, Lu ZJ, Wei YT (2013) Research on modeling of heat source for electron beam welding fusion-solidification zone. *Chin J Aeronaut* 26(1):217–223. <https://doi.org/10.1016/j.cja.2012.12.023>
12. Wang JQ, Han JM, Domblesky JP, Yang ZY, Zhao YX, Zhang Q (2016) Development of a new combined heat source model for welding based on a polynomial curve fit of the experimental fusion line. *Int J Adv Manuf Technol* 87(5–8):1985–1997. <https://doi.org/10.1007/s00170-016-8587-3>
13. Gratkowski S, Brykalski A, Sikora R, Ziolkowski M, Brauer H (2009) Modelling of Seebeck effect in electron beam deep welding of dissimilar metals. *COMPTEL*. <https://doi.org/10.1108/03321640910918940>
14. Petrov P, Tongov M (2020) Numerical modelling of heat source during electron beam welding. *Vacuum* 171:108991. <https://doi.org/10.1016/j.vacuum.2019.108991>
15. Ferro P, Zambon A, Bonollo F (2005) Investigation of electron-beam welding in wrought Inconel 706—experimental and numerical analysis. *Mater Sci Eng A* 392(1):94–105. <https://doi.org/10.1016/j.msea.2004.10.039>
16. Maurer W, Ernst W, Rauch R, Kapl S, Pohl A, Krüssel T, Vallant R, Enzinger N (2012) Electron beam welding of Atmcp steel with 700 mpa yield strength. *Weld World* 56(9–10):85–94. <https://doi.org/10.1007/BF03321384>
17. Sun Z, Karppi R (1996) The application of electron beam welding for the joining of dissimilar metals: an overview. *J Mater Process Technol* 59(3):257–267. [https://doi.org/10.1016/0924-0136\(95\)02150-7](https://doi.org/10.1016/0924-0136(95)02150-7)

18. Venkata KA, Truman CE, Smith DJ, Bhaduri AK (2016) Characterising electron beam welded dissimilar metal joints to study residual stress relaxation from specimen extraction. *Int J Press Vessel Pip* 139:237–249. <https://doi.org/10.1016/j.ijpvp.2016.02.025>
19. Smith DJ, Zheng G, Hurrell PR, Gill CM, Pellereau BME, Ayres K, Goudar D, Kingston E (2014) Measured and predicted residual stresses in thick section electron beam welded steels. *Int J Press Vessel Pip* 120–121:66–79. <https://doi.org/10.1016/j.ijpvp.2014.05.001>
20. Lacki P, Adamus K, Wiczorek P (2014) Theoretical and experimental analysis of thermo-mechanical phenomena during electron beam welding process. *Comput Mater Sci* 94:17–26. <https://doi.org/10.1016/j.commatsci.2014.01.027>
21. Elliott S (1984) Electron beam welding of C–Mn steels—toughness and fatigue properties. *Weld J* 63(1):8. https://app.aws.org/wj/supplement/WJ_1984_01_s9.pdf
22. Li XB, Lu FG, Cui HC, Tang XH, Wu YX (2014) Numerical modeling on the formation process of keyhole-induced porosity for laser welding steel with T-joint. *Int J Adv Manuf Technol* 72(1–4):241–254. <https://doi.org/10.1007/s00170-014-5609-x>
23. Tsirkas SA, Papanikos P, Pericleous K, Strusevich N, Boitout F, Bergheau JM (2003) Evaluation of distortions in laser welded ship-building parts using local-global finite element approach. *Sci Technol Weld Join* 8(2):79–88. <http://gala.gre.ac.uk/id/eprint/626>. <https://doi.org/10.1179/136217103225010899>
24. Carmignani C, Mares R, Toselli G (1999) Transient finite element analysis of deep penetration laser welding process in a singlepass butt-welded thick steel plate. *Comput Methods Appl Mech Eng* 179(3–4):197–214. [https://doi.org/10.1016/S0045-7825\(99\)00043-2](https://doi.org/10.1016/S0045-7825(99)00043-2)
25. Luo X, Shinozaki K, Kuroki H, Yoshihara S, Okumoto Y, Shirai M (2002) Analysis of temperature and elevated temperature plastic strain distributions in laser welding HAZ study of laser weldability of Ni-base superalloys (report 5). *Weld Int* 16(5):385–392. <https://doi.org/10.1080/09507110209549547> <https://www.tandfonline.com/doi/pdf/10.1080/09507110209549547>
26. Chen GQ, Liu JP, Shu X, Gu H, Zhang BG (2019) Numerical simulation of keyhole morphology and molten pool flow behavior in aluminum alloy electron-beam welding. *Int J Heat Mass Transf* 138:879–888. <https://doi.org/10.1016/j.ijheatmasstransfer.2019.04.112>
27. Evdokimov A, Springer K, Doynov N, Ossenbrink R, Michailov V (2017) Heat source model for laser beam welding of steel-aluminum lap joints. *Int J Adv Manuf Technol* 93(1–4):709–716. <https://doi.org/10.1007/s00170-017-0569-6>
28. Nyon KY, Nyeoh CY, Mokhtar M, Abdul-Rahman R (2012) Finite element analysis of laser inert gas cutting on Inconel 718. *Int J Adv Manuf Technol* 60(9–12):995–1007. <https://doi.org/10.1007/s00170-011-3655-1>
29. Hou ZL, Zhao T, Xu Z, Zhu LH, Sun JH, Jin YH, Lv XZ (2019) The new heat source model of AZ31B magnesium alloy laser-TIG hybrid welding. In *Key engineering materials* (Vol. 815, pp. 120–124). Trans Tech Publications Ltd. <https://doi.org/10.4028/www.scientific.net/KEM.815.120>
30. Zhang LW, Pei JB, Zhang QZ, Liu CD, Zhu WH, Qu S, Wang JH (2007) The coupled FEM analysis of the transient temperature field during inertia friction welding of GH4169 alloy. *Acta Metall Sin (Eng Lett)* 20(4):301–306. [https://doi.org/10.1016/S1006-7191\(07\)60043-X](https://doi.org/10.1016/S1006-7191(07)60043-X)
31. Geng PH, Qin GL, Zhou J (2020) A computational modeling of fully friction contact-interaction in linear friction welding of Ni-based superalloys. *Mater Des* 185:108244. <https://doi.org/10.1016/j.matdes.2019.108244>
32. Cook PS, Murphy AB (2019) Simulation of melt pool behaviour during additive manufacturing: underlying physics and progress. *Addit Manuf* 100909. <https://doi.org/10.1016/j.addma.2019.100909>
33. Agnoli A, Bernacki M, Logé R, Franchet JM, Laigo J, Bozzolo N (2015) Selective growth of low stored energy grains during δ sub-solvus annealing in the Inconel 718 nickel-based superalloy. *Metall Mater Trans A* 46(9):4405–4421. <https://doi.org/10.1007/s11661-015-3035-9>
34. Withers PJ, Bhadeshia HKDH (2001) Residual stress. Part 1—measurement techniques. *Mater Sci Technol* 17(4):355–365. <https://doi.org/10.1179/026708301101509980>
35. Withers PJ, Bhadeshia HKDH (2001) Residual stress. Part 2—nature and origins. *Mater Sci Technol* 17(4):366–375. <https://doi.org/10.1179/026708301101510087>
36. Pu XW, Zhang CH, Li S, Deng D (2017) Simulating welding residual stress and deformation in a multi-pass butt-welded joint considering balance between computing time and prediction accuracy. *Int J Adv Manuf Technol* 93(5–8):2215–2226. <https://doi.org/10.1007/s00170-017-0691-5>
37. Brünnet H, Bähre D, Rickert T, Daprich D (2014) Modeling and measurement of residual stresses along the process chain of autofrettaged components by using FEA and hole-drilling method with ESPI. In *Materials Science Forum* (Vol. 768, pp. 79–86). Trans Tech Publications Ltd. <https://doi.org/10.4028/www.scientific.net/MSF.768-769.79>
38. Manson SS (1953) Behavior of materials under conditions of thermal stress (Vol. 2933). National Advisory Committee for Aeronautics. <https://ntrs.nasa.gov/search.jsp?R=19930092197>. <http://hdl.handle.net/2060/19930083626>
39. Coffin LF Jr (1954) A study of the effects of cyclic thermal stresses on a ductile metal. *Trans Am Soc Mech Eng New York* 76:931–950. <https://ci.nii.ac.jp/naid/10012801028/>
40. Wollmann J, Dolny A, Kaszuba M, Gronostajski Z, Gude M (2019) Methods for determination of low-cycle properties from monotonic tensile tests of 1.2344 steel applied for hot forging dies. *Int J Adv Manuf Technol* 102(9–12):3357–3367. <https://doi.org/10.1007/s00170-019-03349-2>

Publisher's note Springer Nature remains neutral with regard to jurisdictional claims in published maps and institutional affiliations.